Journal of Materials Chemistry A

ROYAL SOCIETY OF CHEMISTRY

PAPER

View Article Online
View Journal | View Issue

Cite this: J. Mater. Chem. A, 2021, 9, 9038

A facile method to stabilize sodium metal anodes towards high-performance sodium batteries†

Qiongqiong Lu, *[ab] Ahmad Omar,[a] Ling Ding,[ab] Steffen Oswald,[a] Martin Hantusch,[a] Lars Giebeler,[a] Kornelius Nielsch[abc] and Daria Mikhailova *[a]

Sodium metal is the ultimate anode for next generation high-energy-density sodium metal batteries due to its superior theoretical specific capacity, low redox potential, and natural abundance. However, sodium metal suffers from extreme and uncontrollable dendrite growth and gas evolution problems. These incidents result in a low coulombic efficiency and safety issues such as dangerous short circuits. Herein, an effective protective layer is fabricated on the Na metal anode *via* an extremely facile pretreatment method with 1,3-dioxolane. The protective layer exhibits fast interfacial transport and a lower resistance. Direct optical visualization shows that dendrite growth and gas evolution are suppressed due to the introduction of the protective layer. As a result, an outstanding cycling stability for 2800 h (1400 cycles) at 1 mA cm^{-2} in a symmetric cell is obtained. Moreover, the full cell using the protected Na metal anode shows superior electrochemical performance in comparison to the untreated Na metal anode. Furthermore, large format protected Na metal anodes fabricated by spraying 1,3-dioxolane were demonstrated and successfully assembled in pouch cells, showing a stable specific capacity of around 95 mA h g^{-1}. Thus, our work presents a facile, efficient and scalable protection strategy to stabilize Na metal anodes towards high-energy-density sodium batteries.

Received 4th January 2021
Accepted 11th March 2021

DOI: 10.1039/d1ta00066g

rsc.li/materials-a

Introduction

The development of high-energy-density rechargeable batteries based on advanced electrodes is urgently needed to sustainably meet the growing demand for portable electronics, electric vehicles and smart electrical grids.[1–10] Sodium metal is a superlative anode material for high-energy-density Na metal batteries such as room temperature Na–S,[11–14] Na–Se,[15] Na–O_2,[16,17] and Na–CO_2 [18,19] systems owing to its high theoretical specific capacity (1166 mA h g^{-1}), low redox potential (−2.714 V *vs.* the standard hydrogen electrode), natural abundance, and low cost.[20] However, there are significant scientific and practical challenges associated with it that need to be overcome for the development of the Na metal anode towards applications. The major problem afflicting the Na metal anode is the dendrite growth during the Na plating/stripping process leading to serious safety and lifetime issues.[21] As a result of an irreversible reaction between highly reactive Na and organic electrolytes, a chemically and morphologically heterogeneous solid-electrolyte interface (SEI) is generally formed, which induces an uneven Na deposition resulting in a massive dendrite growth. Moreover, the SEI formed is rather rigid and unstable and undergoes cracking due to volume changes caused by the uneven Na deposition. This behavior further leads to the preferential deposition of Na on the freshly created surfaces, exacerbating the dendrite formation. In addition, the dendrite growth and unstable SEI formation continuously consume the electrolyte, which induces poor coulombic efficiencies (CEs) and ultimately leads to a short cycle life. Furthermore, the dendrites may break or collapse to form dead Na leading to a sudden drop of the CE, an increase in impedance and loss of Na from the electrodes (Fig. 1). Moreover, owing to the high

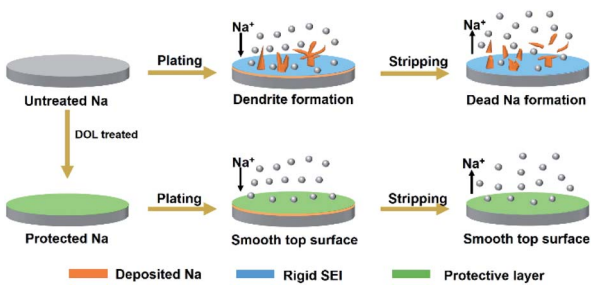

Fig. 1 Schematic illustration of the Na plating and stripping behavior of untreated (upper case) and protected Na (lower case).

[a]Leibniz Institute for Solid State and Materials Research (IFW) Dresden e.V., Helmholtzstraße 20, 01069 Dresden, Germany. E-mail: q.lu@ifw-dresden.de; d.mikhailova@ifw-dresden.de

[b]Institute of Materials Science, Technische Universität Dresden, Helmholtzstraße 7, 01062 Dresden, Germany

[c]Institute of Applied Physics, Technische Universität Dresden, Nöthnitzer Straße 61, 01062 Dresden, Germany

† Electronic supplementary information (ESI) available. See DOI: 10.1039/d1ta00066g

reactivity of Na with the organic components of the electrolyte, the evolution of flammable gases causes severe safety hazards.[22–26]

In recent years, active research has been conducted toward tackling the aforementioned issues. One strategy is to develop Na hosts by designing porous architectures of three-dimensional (3D) current collectors.[27–31] Nevertheless, the reaction between Na and the electrolyte was found to be aggravated because the plated Na duplicated the porous structure of the 3D current collector.[32] Another strategy that has been explored is to tailor electrolyte systems using additives,[33,34] highly concentrated electrolytes,[35] ionic liquids,[36] gels[37] and solid-state electrolytes.[38] However, this approach is challenging because the Na metal is thermodynamically unstable in organic solvents/solid-state electrolytes in addition to the poor diffusion phenomenon in gel and solid-state electrolytes at room temperature.[39] Alternatively, the design of artificial protective layers on the Na surface by coating or through an *in situ* synthesis method has been found to be one of the most promising ways to stabilize Na metal anodes. For instance, NaBr,[40] NaF,[41] NaI,[42] Bi,[43] Na–Sn alloys,[44–46] Al_2O_3,[47,48] graphene,[49] MoS_2,[50] alucone,[51] ionic polymer films[52] and inorganic–organic coatings[53] have been explored to form ionically conductive, mechanically robust and electrochemically stable protective layers. However, most of the protection methods are rather complicated or involve high costs, making them infeasible for scaled up synthesis and practical implementation. In addition, only a few reports demonstrate stable long-term cycling at practical current densities larger than 0.5 mA cm^{-2} and areal capacities higher than 0.5 mA h cm^{-2}. Therefore, it is important to develop an effective protective layer for Na metal anodes through a facile and scalable approach involving inexpensive components and processing methods, in order to facilitate the practical implementation of the Na metal anode in high energy density Na batteries.

One of the approaches in regard to protective layer coating on alkali metals is represented by organic polymerization. 1,3-dioxolane (DOL), a common ether solvent for batteries, is historically known to easily polymerize, and DOL polymerization has been explored in various battery systems. For example, cationic ring-opening polymerization of DOL has been utilized towards polymer gel electrolytes demonstrating high ionic conductivity, compatibility for metal anodes and universality towards different cathode materials.[54–57] In other studies, electro-polymerization of DOL on lithium metal and lithium–tin alloy anodes enabled an improved Li–S battery performance.[58,59] Zhang and coworkers used DOL as an electrolyte additive for preparing a robust and flexible passivating layer of poly(DOL) on a Li–Na alloy.[60] With an optimized Li–Na alloy anode, the formed film suppressed dendrite formation, increased the oxidation resistance and kept the Li–Na alloy anode crack-free. As an alternative approach, Zhou's group reported a direct pretreatment reaction with Li to form a stable protective layer using 1,4-dioxane which has a similar structure to DOL, leading to improved cycling stability in Li–O_2 batteries.[61] However, to the best of our knowledge, there is no report about using DOL for the stabilization of sodium metal anodes in sodium batteries. In addition, Na–S full batteries suffer from more severe polysulfide shuttle problems as compared to Li–S batteries, which puts forward a higher requirement on stable sodium metal anodes.[12,62,63]

In this work, we demonstrate a stable protective layer on Na metal anodes, formed by a simple, effective and low-cost DOL pretreatment method. The protective layer shows a fast interfacial transport and a low charge transfer resistance as well as a low solid-electrolyte interphase resistance. At the same time, it is highly effective in improving the interface stability and suppressing the dendrite growth. As a result, the protected Na electrodes exhibit excellent electrochemical performance in symmetric Na–Na cells. Moreover, with protected Na electrodes, an improved cycling stability in full cells with $Na_3V_2(PO_4)_3$ (NVP) and sulfur cathodes was also proven in comparison to untreated Na electrodes. The ease of applicability and scalability of the pretreated process was further demonstrated through the preparation of large-format protected Na anodes by spray coating, which were successfully implemented in prototypical pouch cells.

Experimental methods

Preparation of untreated and protected Na metal

A bulk Na piece (Alfa Aesar, 99.95%) was taken out from mineral oil and cleaned with a lab tissue. Next, a slice of the Na piece was cut with a knife and rolled into Na foil. After that, the Na foil was punched as 12 mm discs to get Na metal electrodes. For fabricating the protective layer, Na electrodes were soaked for different times (1 min, 5 min, and 10 min) in molecular sieve-dried DOL (BASF) and subsequently dried in a glovebox. All handling and operation steps were performed in an argon-filled glovebox (H_2O and O_2 < 0.1 ppm).

Preparation of the $Na_3V_2(PO_4)_3$ (NVP) cathode

NVP was prepared *via* a sol–gel method. In a typical synthesis, $CH_3COONa\cdot 3H_2O$ (Sigma-Aldrich, ≥99%), NH_4VO_3 (Sigma-Aldrich, ≥99%), $NH_4H_2PO_4$ (Sigma-Aldrich, ≥99%), and citric acid $C_6H_8O_7\cdot H_2O$ (Sigma-Aldrich, ≥99%) were added into deionized water and stirred for 30 min, and then dried at 80 °C overnight in air. The obtained precursor was ground and pretreated at 350 °C for 6 h, and then annealed at 800 °C for 12 h in a tube furnace under an argon flow to obtain NVP powder. For the preparation of NVP electrodes, a slurry composed of the NVP powder, Super C65 (TIMCAL, Switzerland) and polyvinylidene difluoride (PVDF, Solef 21216) in a weight ratio of 8 : 1 : 1 was made, using *N*-methyl-2-pyrrolidone (NMP, Sigma-Aldrich, 99%) as the solvent. The slurry was mixed using a shaker mill (MM200, Retsch) at 25 Hz for 30 min. Afterwards, the slurry was coated with a doctor blade (ZUA2000, Zehntner GmbH) onto Al foil (15 μm thickness, MTI Corp.) using an Erichsen Coatmaster. The coated current collector foil was dried at 110 °C overnight in air. The active material loading was approximately 1.5 mg cm^{-2}, calculated as a weight difference of the Al foil before and after coating by factoring in the weight ratio of the components.

Preparation of the sulfur cathode

The electrode slurry was prepared from sulfur (Aldrich, 99.98%), Super C65 and PVDF in a weight ratio of 7 : 2 : 1 along with NMP as the solvent and mixed using a Retsch shaker mill at 25 Hz for 30 min. Next, the slurry was coated on Cu foil (25 μm thickness, MTI Corp.) using a doctor blade technique. The electrode sheet was punched into disks of 10 mm in diameter after drying at 60 °C overnight in air. The areal sulfur loading of the electrode was approximately 1 mg cm^{-2}, which was calculated by weighing the copper foil before and after coating and factoring in the weight ratio of the components.

Materials characterization

The morphology of the materials and electrodes was characterized by field-emission scanning electron microscopy (FEG-SEM, Zeiss-Leo Gemini 1530). Elemental analysis was performed using energy dispersive X-ray spectroscopy (EDXS) with a SEM-coupled Bruker XFlash 6 detector. To reduce the exposure of Na electrodes in air, a home-made transfer system was utilized to transport the samples from the argon-filled glovebox to the SEM. The exposure was minimized to a few seconds during transfer to the SEM chamber and the subsequent evacuation. For post-mortem SEM investigations after cycling, the electrodes were washed with dimethyl ether, followed by drying, both inside a glovebox. The phase purity and the structure of the samples were characterized by X-ray powder diffraction (XRD) with a STOE STADI P diffractometer equipped with a Mythen 1K detector, using Cu $K_{\alpha 1}$ and Mo $K_{\alpha 1}$ radiations. Fourier transform infrared (FTIR) spectroscopy (Nicolet 6700, Thermo Scientific) was carried out in attenuated total reflection (ATR) mode. For the FTIR investigations on the electrodes after cycling, they were washed with tetraethylene glycol dimethyl ether, followed by drying inside a glovebox. X-ray photoelectron spectroscopy (XPS) was performed on a PHI 5600 CI (Physical Electronics) instrument. An Al K_α X-ray source (350 W) was used at a pass energy of 29 eV for C 1s and Na 1s spectra. Since with the Al K_α X-ray source the O 1s spectrum overlaps with the Na 1s spectrum, a 400 W Mg K_α X-ray source at a pass energy of 29 eV was applied to obtain a high-resolution O 1s spectrum. A transfer chamber (PHI model 04-110) was used for the transport of samples from the glovebox to the spectrometer avoiding any contact with air and moisture. The binding energy scale was calibrated with the artificial C 1s peak maximum at 284.8 eV for sp^2 carbon. *In situ* optical microscopy for Na deposition and gas evolution studies was performed with a DM4 digital microscope (Baisite, China) coupled with a LAND-CT2001A (Wuhan LAND Electronic Co. Ltd, China) potentiostat. The cell setup for the *in situ* visualization of the Na surface cross section consisted of a cuvette with a Teflon cap, and two stainless steel rods used as current collectors for attaching the Na electrodes. The cap is well-sealed with Parafilm to prevent electrolyte leakage and evaporation as well as humid air intrusion. An optical microscopy cell was also assembled in an Ar-containing, moisture- and oxygen-monitored glovebox.

Symmetric cell tests

Symmetric cells were assembled in CR2025-type coin cell housings and measured with a VMP3 (Biologic, France) potentiostat. For each cell, identical untreated Na or protected Na served as both the working electrode and the counter electrode. 1 M $NaPF_6$ (Alfa Aesar, ≥99%) in tetraethylene glycol dimethyl ether (TEGDME) (Sigma-Aldrich, ≥99%) and a Celgard 2500 were used as the electrolyte and separator, respectively. Galvanostatic cycling was performed with different current densities starting from 1 mA cm^{-2} to 3 mA cm^{-2}. Cyclic voltammetry (CV) was conducted in a voltage range of $-0.2\ V \leq U \leq 0.2\ V$ *vs.* Na/Na^+ with a scan rate of 1 mV s^{-1}. Electrochemical impedance spectroscopy (EIS) was performed in the frequency range from 100 kHz to 10 mHz using a 5 mV AC voltage amplitude. All measurements were conducted at 25 °C using specialized climate chambers.

Full cell tests

Full cells were built using untreated Na or protected Na, and NVP and sulfur electrodes as cathodes. 1 M $NaPF_6$ in TEGDME was used as the electrolyte and a Celgard 2500 was used as the separator. Galvanostatic cycling was performed using a LAND-CT2001A potentiostat. All cells were cycled in a voltage range of $2.5\ V \leq U \leq 4.0\ V$ *vs.* Na/Na^+ for the Na//NVP cell and $0.1\ V \leq U \leq 3.0\ V$ *vs.* Na/Na^+ for the Na//S cell.

Pouch cell assembly

The pouch cells were also assembled in an argon-filled glovebox (H_2O and O_2 < 0.1 ppm). The size of both the NVP cathode and Na metal anode was 5 cm × 4 cm. A protected Na metal anode for the pouch cell was prepared by spraying DOL with a rate of 0.4 mL min^{-1} for 5 min inside the glovebox, where it was subsequently dried. Aluminum strips were attached on both electrodes and the pouch cell stack was assembled with a Celgard 2500 as the separator. After electrolyte (1 M $NaPF_6$ in TEGDME) infiltration, the cells were sealed in aluminum composite foil inside the glovebox using a vacuum sealing machine (KMS Automation, Germany).

Results and discussion

The protected Na metal anode was prepared by a simple pretreatment route through soaking in DOL for 5 min, as schematically shown in Fig. 2a. Although reports on DOL interaction with Na metal are very limited, it is well known that DOL polymerizes in the presence of Li to form a polymer (poly (DOL)).[64–67] Due to the similar electronegativities and first ionization energies of Li and Na, a similar reaction pathway is expected for the reaction of Na with DOL. In analogy to the reaction pathway between DOL and Li, a scheme for the reaction between DOL and Na is proposed, given in Fig. S1.† First, as shown in Path 1, the polar C–O bond in DOL is broken, generating aliphatic sodium alkoxides ($CH_3OCH_2CH_2ONa$ and $CH_3CH_2OCH_2ONa$) and HCOONa. Subsequently, RONa is produced from the reaction between aliphatic sodium alkoxides and Na. HCOONa and RONa, being nucleophiles (labeled with

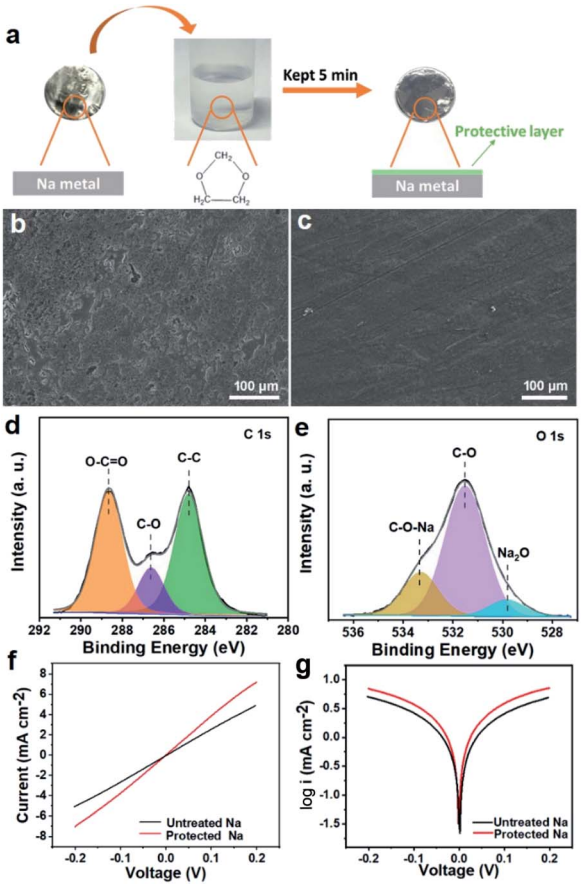

Fig. 2 (a) schematic illustration of the fabrication of protected Na. SEM images of (b) untreated Na and (c) protected Na. High resolution XP spectra of (d) C 1s and (e) O 1s of protective Na recorded with an Al source and Mg source, respectively. (f) Linear part of the CV curves and (g) Tafel plots of the symmetric cell with untreated Na and protected Na as electrodes.

pink boxes), would continuously react with DOL. Finally, poly(DOL) is expected to be generated, as shown in Path 2. To investigate the effect of the treatment time, symmetric cells of protected Na with various treatment times were evaluated (Fig. S2†). Due to the lowest overpotential of protected Na with a treatment time of 5 min, we finally selected the treatment time of 5 min for the subsequent experiments.

The surface composition of the protected Na metal was investigated by Energy Dispersive X-ray Spectroscopy (EDXS), X-ray photoelectron spectroscopy (XPS) and Fourier transform infrared spectroscopy (FTIR). EDXS investigation showed a higher concentration of C and O on the surface of protected Na, due to the organic layer formation (Fig. S3†). Similar results on the surface elemental compositions are obtained by XPS, which confirmed the higher content of C on the surface of protected Na (Table S1†). The elements C and O on the surface of untreated Na are likely related to residues from the mineral oil and reaction with traces of O_2 and H_2O. High resolution XP spectra were recorded for both samples. Fig. 2d and e show the C 1s and O 1s spectra for protected Na. In the C 1s spectrum, three different contributions of C species were found with the maximum at 284.8 eV, 286.6 eV and 288.6 eV. Compared to the literature, the peak at 284.8 eV corresponds to the aliphatic carbon (C–C) groups of organic compounds.[59] Accordingly, the binding energy at 286.6 eV is ascribed to the C–O groups of poly(DOL).[61,66,68,69] In contrast to the protected Na, only small quantities of C–O species were present in the C 1s spectrum of untreated Na (Fig. S4a†). Additionally, the species at 288.6 eV are related to the O–C=O group of HCOONa, which represents a by-product of the DOL reduction by Na, similar to what has been reported for the same reaction of DOL with Li.[66] In the O 1s spectrum, three significant contributions were detected at 529.8 eV, 531.5 eV and 533.3 eV that correspond to the Na–O bond of Na_2O, and to C–O and C–O–Na in the organic polymer layer, respectively.[70] Small quantities of Na_2O are also present in the protective layer due to the reaction of Na with either completely removed oxygen atoms from the DOL decomposition or residual surface OH groups. In contrast, the C–O species were not found in the O 1s spectrum of untreated Na (Fig. S4b†), as no poly(DOL) is located at the surface. The observed characteristic FTIR signals at 1078 cm^{-1} and 1454 cm^{-1}, respectively, correspond to C–O stretching and C–H bending vibrations, and further confirm the formation of RONa/poly(DOL) with –ONa edge groups on the surface of the protected Na metal (Fig. S5†).[65] These results show that there is indeed a formation of a polymerized layer on the surface of the Na metal, mainly consisting of poly(DOL)-type species. Thus, poly(DOL) that forms on the surface of Na is expected to act as an elastic and robust protective layer towards the stabilization of the Na metal for utilization as an anode in Na batteries. As shown by SEM images in Fig. 2b and S3a,† untreated Na has a microscale rough, pitted surface following its brief exposure to air and moisture during shifting from the transfer system to the SEM stage. In contrast, protected Na is characterized by a smooth surface (Fig. 2c and S3c†), understood to be a result of an improved shielding from air and moisture exposure owing to a homogeneous robust barrier layer that poly(DOL) is able to provide.

To evaluate the electrochemical performance of protected Na in comparison to untreated Na, symmetric cell setups were used. 1 M $NaPF_6$ in TEGDME was chosen as the electrolyte, as this ether-based electrolyte is stable and usually used for high-energy-density batteries (sodium–sulfur batteries and sodium–oxygen batteries). Fig. 2f shows the linear part of cyclic voltammetry (CV) curves, where protected Na shows steeper slopes than untreated Na. From the corresponding Tafel plots calculated according to the Tafel extrapolation method (Fig. 2j), a higher exchange current density (1.20 mA cm^{-2}) is observed for protected Na as compared to untreated Na (0.71 mA cm^{-2}), which highlights fast charge transfer kinetics for the protected Na compared to the untreated Na.[43,71] Furthermore, electrochemical impedance spectroscopy (EIS) was performed on symmetric cells before and after cycling at a current density of 2 mA cm^{-2} with a capacity of 1 mA h cm^{-2}. The Nyquist plots are given in Fig. S6 of the ESI,† along with the equivalent circuit models used for fitting to obtain the charge transfer resistance (R_{ct}) along with the solid electrolyte interphase resistance (R_{SEI}). The results are summarized in Table S2.† As compared to

untreated Na, protected Na exhibits a lower R_{ct} and a low R_{SEI} value as well, both before and after cycling. The results further imply that the protective layer supports a faster ion transport. The improvement in ion transport may be ascribed to the improved electrolyte wettability and the polar groups of protective layer coordinating Na^+ (Fig. S7†).[72]

The cycling performance of untreated Na and protected Na was evaluated at an areal capacity of 1 mA h cm^{-2} at different current densities (1 mA cm^{-2}, 2 mA cm^{-2} and 3 mA cm^{-2}) for galvanostatic stripping and plating (Fig. 3a–c). Particularly at a current density of 1 mA cm^{-2}, untreated Na shows quite unstable cycling with increasing overpotential from 25 mV to 330 mV in the first 200 h, due to an unstable and inhomogeneous SEI. In contrast, protected Na performs with an excellent stability for 2800 h or 1400 cycles. Additionally, protected Na (inset in Fig. 3a) exhibits flat voltage profiles and only a small overpotential (~25 mV) over the entire cycling time range. This result overperforms those reported in the literature on Na metal anodes with protective layers by up to almost three times (Table S3†), and the improved performance is even retained for higher current densities as well. At 2 mA cm^{-2} and 3 mA cm^{-2}, protected Na demonstrates significantly better performances with flat voltage profiles and small overpotentials (~50 mV at 2 mA cm^{-2} over 380 h and ~100 mV at 3 mA cm^{-2} over 130 h). The results for the untreated Na are in contrast to those of the protected one with significantly higher overpotentials (~160 mV at 2 mA cm^{-2} and ~420 mV at 3 mA cm^{-2}) and unstable voltage profiles (see the insets of Fig. 3b and c). Therefore, the outstanding electrochemical performance is a clear validation of the presented facile Na anode protection strategy that results in a stabilizing effect on the Na metal anode during cycling in symmetric cell setups. The already highlighted differences are well-supported by the morphological changes of the metal surface of the protected Na electrodes in comparison to untreated Na. Samples of both electrodes after 20 charging and discharging cycles were investigated by SEM (Fig. 3d and e). Here, the untreated Na surface shows a rough and porous morphology like a shrubby crustose lichen but with relatively sharp edges and pikes corresponding to a high ability to form dendrites (Fig. 3d). After the same cycling procedure, the surface of the protected Na is compact and smooth with less porosity, highlighting the effectiveness of the protective layer in suppressing morphological changes and dendrite growth after repeated Na plating and stripping (Fig. 3e). For closer investigation of the stripping and plating mechanism, *in situ* optical microscopy, as one of the best ways to directly observe the dendrite growth and gas evolution on metal anodes, was chosen. For that purpose, specialized cells were assembled using transparent cuvettes (Fig. 4a and b). A current density of 3 mA cm^{-2} was applied to the cells to enhance the dendrite growth for an easier resolution, which were simultaneously monitored with a digital microscope. Fig. 4c shows the photographs taken at a time interval of 15 min for 1 h. Before cycling,

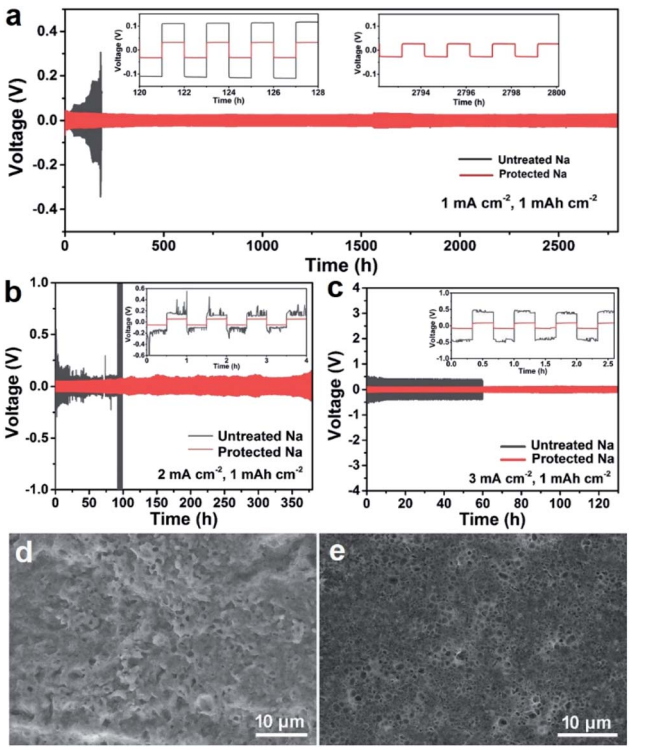

Fig. 3 Voltage profiles of symmetric cells of untreated and protected Na at current densities of (a) 1 mA cm^{-2}, (b) 2 mA cm^{-2} and (c) 3 mA cm^{-2} with a capacity of 1 mA h cm^{-2} in a 1 M $NaPF_6$ in TEGDME electrolyte. The insets show the high-resolution voltage profiles at a specific time. SEM images of (d) untreated Na and (e) protected Na after 20 cycles at a current density of 2 mA cm^{-2} with a capacity of 1 mA h cm^{-2}.

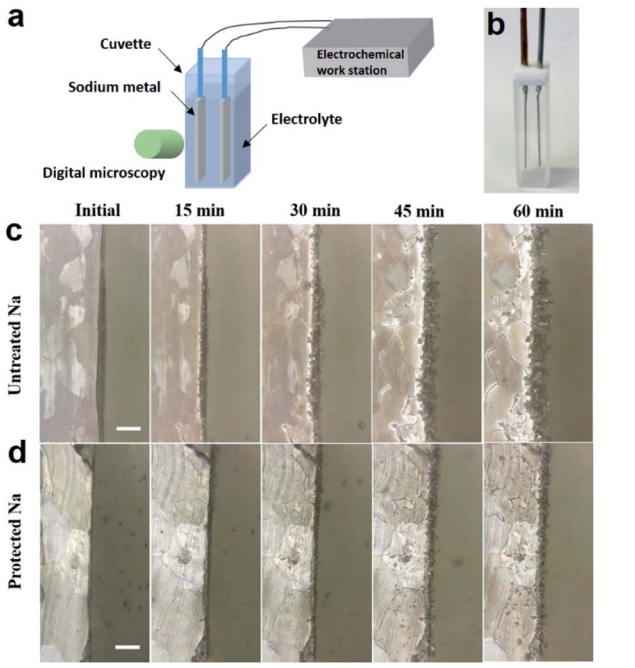

Fig. 4 (a) Schematic diagram of the cell set-up for *in situ* microscopy observation on Na deposition. (b) The photograph of the transparent cell for *in situ* visualization of Na deposition. *In situ* digital microscopic images of the surface cross section of (c) untreated Na and (d) protected Na, recorded at different deposition times. The scale bar is 0.5 mm, applicable to all images.

the surface of both electrodes, untreated Na and protected Na, is smooth as cut. During the plating process protrusions start to appear along the edges of the untreated Na electrode, indicating an uneven Na deposition representing a typical dendritic growth in its multi-branched almost tree-like morphology, well developed after 60 min. In sharp contrast, the protected Na shows only tiny protrusions and therewith a minimal growth. Therefore, dendrite growth inhibition by the protective layer on Na metal was successfully detected on a visually documented microscopic scale. In addition to the dendrite suppression by a mechanically robust layer, the polar oxygen containing groups of the protective poly(DOL) layer, as confirmed by XPS and FTIR, may further support a uniform Na^+ ion deposition, contributing to an improved surface smoothness after cycling as shown by SEM in Fig. 3e.[73] As can be seen in the FTIR spectrum of protected Na after cycling, the characteristic signals of the protective layer are retained, indicating the durability of the protective layer during cycling (Fig. S8†). Since the coating is polymeric, it sustains Na^+ transport through it as well as maintaining its affinity with the Na metal during cycling. In addition, the high viscosity of TEGDME further suppresses the dissolution of the polymeric coating in the electrolyte. To further study the stabilization of interfaces by the protective layer on Na, the gas evolution under solvent-only and under electrolyte conditions was investigated by soaking untreated and protected Na in both TEGDME and the electrolyte (1 M $NaPF_6$ in TEGDME) since Na is highly reactive to the electrolyte components. Fig. 5 shows the photographs of the cross section for both untreated Na and protected Na taken at 1 min and 2 min time intervals for TEGDME and the electrolyte, respectively. With the pure TEGDME solvent, untreated Na shows a notable gas formation after the direct beginning of the experiment, while the gas evolution was noticeably reduced for protected Na (Fig. 5a). In the case of soaking in the electrolyte, no visible gas bubbles were observed near the surface of the protected Na compared to the untreated Na, further corroborating the stabilization of interfaces by the protective layer (Fig. 5b). In this context the high CE of the protected Na anode is explained, as the side reactions are minimized and therefore no additional consumption of the electrolyte for reactions with fresh Na surfaces occurs. This observation also illustrates the stable cycling of the protected Na anode that can be traced back to only a marginal reformation necessity of the SEI over long cycling durations. The aforementioned results distinctly confirm the stabilizing effect of the protective layer mainly consisting of poly(DOL) at the beginning. The poor performance of untreated Na is mainly due to a non-stable SEI, which is often formed due to continued formation of fresh Na surfaces. Additionally, the rough plating leads to changes in the overpotentials in several spots on the freshly deposited Na leading to significant and unavoidable dendrite growth. The protective coating formed through treatment with DOL not only improved the interfacial kinetics and stability of the SEI, but also led to more uniform Na plating and stripping, thereby significantly minimizing the dendrite growth.

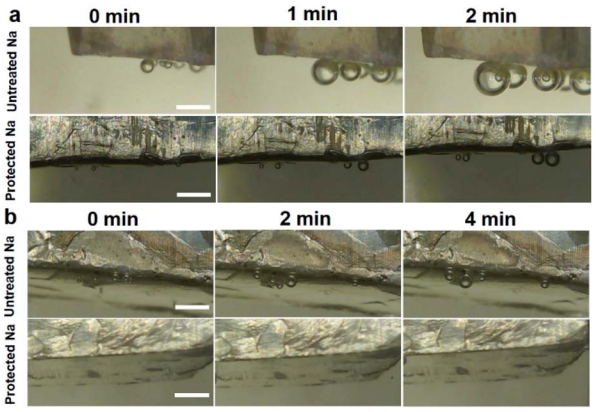

Fig. 5 *In situ* digital micrograph images of the cross-sectional surface of untreated Na and protected Na in (a) TEGDME solvent and (b) the electrolyte (1 M $NaPF_6$ in TEGDME), recorded at different times. The scale bar is 0.5 mm, applicable to all images.

In order to demonstrate the potential of the protected Na for practical applications, it is necessary to evaluate its performance in full cells. Hence, $Na_3V_2(PO_4)_3$ (NVP) and sulfur were chosen as representative cathode materials. Full cells with a protected Na anode are henceforth denoted as P–Na//NVP or P–Na//S (Fig. 6a). As a control, full cells with an untreated Na anode are henceforth referred to as U–Na//NVP or U–Na//S for NVP and sulfur, respectively. High-quality, phase pure NVP (Fig. S9a and S10a†) was synthesized by a sol–gel process, which has been reported elsewhere, and the active material slurry was coated onto Al foil.[74,75] As shown in Fig. 6b–d, P–Na//NVP batteries deliver a stable performance with a high initial discharge capacity of 102 mA h g^{-1}, a high capacity retention of 94 mA h g^{-1} after 200 cycles with an average CE of 99.5% at 0.5C, and a negligible variance after the initial 30 cycles. As a comparison, U–Na//NVP batteries show an initial discharge capacity of 97 mA h g^{-1}, and a noticeable capacity fade, retaining only 86 mA h g^{-1} capacity after 200 cycles, with an unstable and lower CE reaching only a maximum of 95% at the end of 200 cycles (Fig. 6d). The improved capacity of P–Na//NVP batteries is ascribed to their lower charge resistance (Fig. S11†). The P–Na//NVP battery also shows a higher rate capability along with a higher CE, *e.g.*, a higher capacity of 80 mA h g^{-1} for P–Na//NVP and 75 mA h g^{-1} for U–Na//NVP at a high current density of 5C (Fig. S12†). The phenomenon of capacity fluctuation with unstable CE in the long-term cycling of U–Na//NVP is a common issue due to an unstable SEI, continuously reformed on the novel Na metal surface due to inhomogeneous plating and resulting massive dendrite growth, as has been reported previously for NVP cathodes in ether-based electrolytes.[76,77] From the selected discharge/charge profiles as shown in Fig. 6b, the polarization between the charge and discharge plateaus of U–Na//NVP batteries sharply increases after 60 cycles while the change in the polarization for P–Na//NVP is negligible. Here, the change of the polarization of U–Na//NVP cells acts as an indicator of unstable interfaces and dendrite growth on the untreated Na surface. This behavior is further reflected in a sudden drop of the capacity in the 60th cycle (Fig. 6d). The constant polarization of the P–Na//NVP battery confirms that

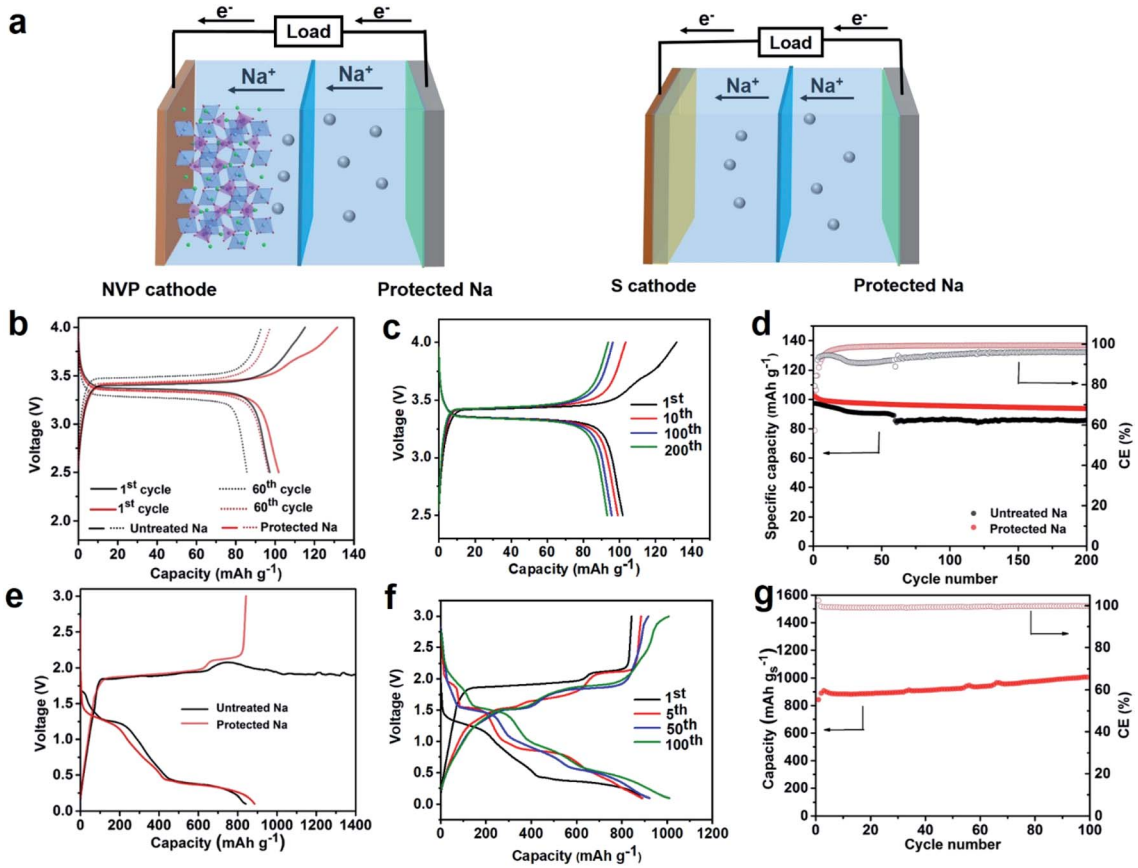

Fig. 6 Electrochemical performance of full cells using untreated Na and protected Na as anodes, respectively. (a) Full cell configurations of P–Na//$Na_3V_2(PO_4)_3$ and P–Na//S batteries. (b) Selected charge/discharge profiles of the 1st and 60th cycles of Na//$Na_3V_2(PO_4)_3$ batteries with different anodes at 0.5C (1C = 118 mA g^{-1}). (c) Charge/discharge curves of P–Na//$Na_3V_2(PO_4)_3$ batteries at 0.5C. (d) Cycling stability of Na//$Na_3V_2(PO_4)_3$ batteries with different anodes at 0.5C.(e) Initial discharge/charge profiles of Na–S batteries with different anodes at 0.5C (1C = 1672 mA g^{-1}). (f) Discharge/charge curves of P–Na//S batteries at 0.5C. (g) Cycling stability of P–Na//S batteries at 0.5C.

the protective layer on the Na anode is highly effective towards improving interfacial stability on the Na metal surface.

For the Na/sulfur cells, sulfur electrodes were similarly prepared and cast on Cu foil since Cu demonstrates a higher effectiveness towards trapping polysulfides.[78] Morphological and structural characterization was performed by XRD and SEM (Fig. S9b and S10b†). Due to the affinity of Cu to sulfur, sulfur was partially converted to CuS on the copper foil during the electrode drying process, which was identified by XRD, and showed the morphology of micro-flowers as visualized in the SEM images. Therefore, in the tested cathode for sulfur batteries, the active material of the sulfur electrode represents a combination of sulfur and CuS. U–Na//S starts with an initial discharge capacity of 842 mA h g^{-1} but suffers from a significant shuttle effect during the charging process (Fig. 6e). The strong shuttle effect is due to the redox reaction of polysulfides, migrating between the two electrodes, and Na dendrite growth which cannot be prevented by the rigid SEI formed on the untreated Na anode. One strategy to mitigate this issue was adopted by Li *et al.* by using three layers of separators (glass fiber/Celgard 2400/glass fiber), which is not suitable for practical applications.[79] In contrast to this, the P–Na//S battery exhibits superior initial discharge and charge capacities of 886 mA h g^{-1} and 842 mA h g^{-1} at 0.5C, respectively, showing high reversibility for at least 100 charge and discharge cycles (Fig. 6e–g). Compared to U–Na//S cells, P–Na//S not only allows for cycling with a single Celgard separator, but also shows a stable cycling performance with a capacity of ~1000 mA h g^{-1} for 100 cycles at 0.5C (Fig. 6f and g). The increased capacity of P–Na//S is attributed to the conversion of S and CuS to Cu_2S after a few cycles, corresponding to the change of the platform in voltage profiles after different cycles (Fig. 6f).[80] These results demonstrated that the protection strategy is highly effective towards superior electrochemical performance in Na batteries with completely different battery chemistries.

To show the possibility of an exceptionally easy upscaling, a protected Na anode was implemented at a prototypical pouch cell level with a NVP cathode. For the purpose of preparing large-format protected Na electrodes, spray coating of DOL was employed, which is a widely used coating technology in the industry (Fig. 7a). Protected Na foil ($L \times W = 5$ cm $\times$ 4 cm) was prepared by spraying DOL with a spray rate of 0.4 mL min^{-1}. According to the FTIR measurement shown in Fig. S13,† the characteristic vibrations of poly(DOL) on the protected Na

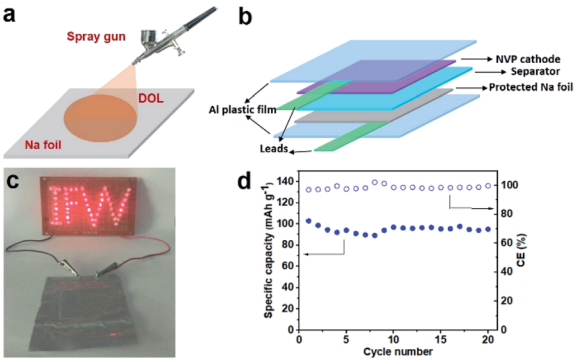

Fig. 7 (a) Schematic diagram of the spraying process to protect Na foil. (b) Schematic diagram of a P–Na//$Na_3V_2(PO_4)_3$ pouch cell. (c) IFW logo (53 LEDs) powered by a P–Na//$Na_3V_2(PO_4)_3$ pouch cell. (d) Cycling performances of the P–Na//$Na_3V_2(PO_4)_3$ pouch cell at 0.1C.

fabricated by spray coating are quite similar to those of protected Na prepared *via* soaking, confirming a successful formation of the protective polymer layer. After drying the protected Na electrode, a pouch cell was assembled with the NVP cathode (Fig. 7b). The P–Na//NVP pouch cell can successfully power an "IFW" shaped light consisting of 53 LEDs (Fig. 7c). Fig. 7d shows the cycling performances of the P–Na//NVP pouch cell at 0.1C. The pouch cells show a discharge specific capacity of 102 mA h g^{-1} corresponding to a capacity of 2.8 mA h in the initial cycle. Furthermore, a stable specific capacity of 95 mA h g^{-1} corresponding to a capacity of 2.6 mA h was obtained till 20 cycles. The results demonstrated that our approach is easily scalable towards stable Na metal anodes and is able to bridge the typical and very critical gap between different cell formats, from a coin cell to a pouch cell with an area of 20 cm^2. The easy and cost-effective integration of spray coating into a roll-to-roll fabrication of electrodes may allow for a continuous and large-scale manufacturing of protected Na anodes.

Conclusions

We have here demonstrated that a protective layer is formed on Na metal by the polymerization of DOL during a pretreatment step, leading to a stable Na metal anode. The fabrication process is straightforward, without the need for any additional catalyst or equipment, making it viable for industrial scalability. The protective layer composed of poly(DOL) on the Na metal enables fast ion transport and exhibits low charge transfer and SEI resistances, reduces morphological changes, regulates the flux and distribution of Na^+ ions and significantly suppresses dendrite growth and gas evolution. As a consequence, excellent cycling in Na–Na symmetric cells is observed at different current densities up to 3 mA g^{-1}. Ultra-long cycling of up to at least 2800 h with a flat voltage profile and a very small overpotential of ~25 mV was obtained for the protected Na at a current density of 1 mA cm^{-2} with an areal capacity of 1 mA h cm^{-2}. The protected Na electrodes were successfully used in full cells with both $Na_3V_2(PO_4)_3$ (NVP) and sulfur cathodes, which show significantly improved capacity performances and cycling stabilities compared to the corresponding cells with untreated Na as the anode. With prototypical pouch cells, the potential scalability of the protection strategy by spray coating was also successfully demonstrated. The results clearly confirm the effectiveness of the DOL pretreatment strategy making Na metal anodes highly promising for practical applications. They also demonstrate high potential for industrial implementation of the process. The proof-of-principle established here paves the way for future studies, *e.g.* exploring substituted DOL and its analogues, to propitiously realize practical Na metal batteries.

Conflicts of interest

There are no conflicts to declare.

Acknowledgements

The authors thank Ronny Buckan, Andrea Voβ, and Anne Voidel (all of them from IFW Dresden) for technical support. Q. L. and L. D. acknowledge the financial support from the China Scholarship Council (CSC). This work was supported by the European Union (European Regional Development Fund-ERDF) and the Free State of Saxony for the NaSBattSy project (SAB Grant No. 100234960). A. O. would like to acknowledge the financial support from the Federal Ministry of Education and Research (BMBF) under the project "KaSiLi" (03XP0254D) in the competence cluster "ExcellBattMat". Dr Rita Barros Leones (IFW Dresden) is acknowledged for helpful discussion. Steffi Kaschube (IFW Dresden) is thanked for help with the XPS measurements.

Notes and references

1 H. Pan, Y.-S. Hu and L. Chen, *Energy Environ. Sci.*, 2013, **6**, 2338–2360.
2 L. Li, Y. Zheng, S. Zhang, J. Yang, Z. Shao and Z. Guo, *Energy Environ. Sci.*, 2018, **11**, 2310–2340.
3 P. K. Nayak, L. Yang, W. Brehm and P. Adelhelm, *Angew. Chem., Int. Ed.*, 2018, **57**, 102–120.
4 X. Xiang, Q. Lu, M. Han and J. Chen, *Chem. Commun.*, 2016, **52**, 3653–3656.
5 S. Wang and X.-B. Zhang, *Adv. Mater.*, 2019, **31**, 1805432.
6 T. Sun, Z.-J. Li, H.-G. Wang, D. Bao, F.-L. Meng and X.-B. Zhang, *Angew. Chem., Int. Ed.*, 2016, **55**, 10662–10666.
7 Y.-H. Zhu, Y.-B. Yin, X. Yang, T. Sun, S. Wang, Y.-S. Jiang, J.-M. Yan and X.-B. Zhang, *Angew. Chem., Int. Ed.*, 2017, **56**, 7881–7885.
8 Y.-H. Zhu, Q. Zhang, X. Yang, E.-Y. Zhao, T. Sun, X.-B. Zhang, S. Wang, X.-Q. Yu, J.-M. Yan and Q. Jiang, *Chem*, 2019, **5**, 168–179.
9 Y.-H. Zhu, X. Yang, D. Bao, X.-F. Bie, T. Sun, S. Wang, Y.-S. Jiang, X.-B. Zhang, J.-M. Yan and Q. Jiang, *Joule*, 2018, **2**, 736–746.
10 T. Sun, Z.-J. Li and X.-B. Zhang, *Research*, 2018, **2018**, 1936735.
11 A. Manthiram and X. Yu, *Small*, 2015, **11**, 2108–2114.

12 Y. X. Wang, B. Zhang, W. Lai, Y. Xu, S. L. Chou, H. K. Liu and S. X. Dou, *Adv. Energy Mater.*, 2017, **7**, 1602829.
13 B.-W. Zhang, T. Sheng, Y.-D. Liu, Y.-X. Wang, L. Zhang, W.-H. Lai, L. Wang, J. Yang, Q.-F. Gu and S.-L. Chou, *Nat. Commun.*, 2018, **9**, 4082.
14 Q. Lu, X. Wang, J. Cao, C. Chen, K. Chen, Z. Zhao, Z. Niu and J. Chen, *Energy Storage Mater.*, 2017, **8**, 77–84.
15 Y. Yao, M. Chen, R. Xu, S. Zeng, H. Yang, S. Ye, F. Liu, X. Wu and Y. Yu, *Adv. Mater.*, 2018, **30**, 1805234.
16 S. K. Das, S. Lau and L. A. Archer, *J. Mater. Chem. A*, 2014, **2**, 12623–12629.
17 B. Sun, C. Pompe, S. Dongmo, J. Zhang, K. Kretschmer, D. Schröder, J. Janek and G. Wang, *Adv. Mater. Technol.*, 2018, **3**, 1800110.
18 X. Hu, J. Sun, Z. Li, Q. Zhao, C. Chen and J. Chen, *Angew. Chem., Int. Ed.*, 2016, **55**, 6482–6486.
19 J. Sun, Y. Lu, H. Yang, M. Han, L. Shao and J. Chen, *Research*, 2018, **2018**, 6914626.
20 H. Wang, E. Matios, J. Luo and W. Li, *Chem. Soc. Rev.*, 2020, **49**, 3783–3805.
21 J. Luo, X. Lu, E. Matios, C. Wang, H. Wang, Y. Zhang, X. Hu and W. Li, *Nano Lett.*, 2020, **10**, 7700–7708.
22 Y. Zhao, K. R. Adair and X. Sun, *Energy Environ. Sci.*, 2018, **11**, 2673–2695.
23 X. Zheng, C. Bommier, W. Luo, L. Jiang, Y. Hao and Y. Huang, *Energy Storage Mater.*, 2018, **16**, 6–23.
24 B. Sun, P. Xiong, U. Maitra, D. Langsdorf, K. Yan, C. Wang, J. Janek, D. Schröder and G. Wang, *Adv. Mater.*, 2020, **32**, 1903891.
25 C. Zhang, A. Wang, J. Zhang, X. Guan, W. Tang and J. Luo, *Adv. Energy Mater.*, 2018, **8**, 1802833.
26 B. Lee, E. Paek, D. Mitlin and S. W. Lee, *Chem. Rev.*, 2019, **119**, 5416–5460.
27 S. Liu, S. Tang, X. Zhang, A. Wang, Q.-H. Yang and J. Luo, *Nano Lett.*, 2017, **17**, 5862–5868.
28 Y. Xu, A. S. Menon, P. P. R. Harks, D. C. Hermes, L. A. Haverkate, S. Unnikrishnan and F. M. Mulder, *Energy Storage Mater.*, 2018, **12**, 69–78.
29 S.-S. Chi, X.-G. Qi, Y.-S. Hu and L.-Z. Fan, *Adv. Energy Mater.*, 2018, **8**, 1702764.
30 A. Wang, X. Hu, H. Tang, C. Zhang, S. Liu, Y. W. Yang, Q. H. Yang and J. Luo, *Angew. Chem., Int. Ed.*, 2017, **56**, 11921–11926.
31 Q. Lu, X. Wang, A. Omar and D. Mikhailova, *Mater. Lett.*, 2020, **275**, 128206.
32 X. Liang, Q. Pang, I. R. Kochetkov, M. S. Sempere, H. Huang, X. Sun and L. F. Nazar, *Nat. Energy*, 2017, **2**, 17119.
33 H. Wang, C. Wang, E. Matios and W. Li, *Angew. Chem., Int. Ed.*, 2018, **57**, 7734–7737.
34 Y. Lee, J. Lee, J. Lee, K. Kim, A. Cha, S. Kang, T. Wi, S. J. Kang, H.-W. Lee and N.-S. Choi, *ACS Appl. Mater. Interfaces*, 2018, **10**, 15270–15280.
35 J. Zheng, S. Chen, W. Zhao, J. Song, M. H. Engelhard and J.-G. Zhang, *ACS Energy Lett.*, 2018, **3**, 315–321.
36 M. Forsyth, H. Yoon, F. Chen, H. Zhu, D. R. MacFarlane, M. Armand and P. C. Howlett, *J. Phys. Chem. C*, 2016, **120**, 4276–4286.
37 X. Hu, P. H. Joo, H. Wang, E. Matios, C. Wang, J. Luo, X. Lu, K. Yang and W. Li, *Adv. Funct. Mater.*, 2019, **29**, 1807974.
38 X. Fan, J. Yue, F. Han, J. Chen, T. Deng, X. Zhou, S. Hou and C. Wang, *ACS Nano*, 2018, **12**, 3360–3368.
39 K. Liao, S. Wu, X. Mu, Q. Lu, M. Han, P. He, Z. Shao and H. Zhou, *Adv. Mater.*, 2018, **30**, 1705711.
40 S. Choudhury, S. Wei, Y. Ozhabes, D. Gunceler, M. J. Zachman, Z. Tu, J. H. Shin, P. Nath, A. Agrawal, L. F. Kourkoutis, T. A. Arias and L. A. Archer, *Nat. Commun.*, 2017, **8**, 898.
41 S. Wu, Y. Qiao, K. Jiang, Y. He, S. Guo and H. Zhou, *Adv. Funct. Mater.*, 2018, **28**, 1706374.
42 H. Tian, H. Shao, Y. Chen, X. Fang, P. Xiong, B. Sun, P. H. L. Notten and G. Wang, *Nano Energy*, 2019, **57**, 692–702.
43 M. Ma, Y. Lu, Z. Yan and J. Chen, *Batteries Supercaps*, 2019, **2**, 663–667.
44 X. Zheng, H. Fu, C. Hu, H. Xu, Y. Huang, J. Wen, H. Sun, W. Luo and Y. Huang, *J. Phys. Chem. Lett.*, 2019, **10**, 707–714.
45 Q. Chen, H. He, Z. Hou, W. Zhuang, T. Zhang, Z. Sun and L. Huang, *J. Mater. Chem. A*, 2020, **8**, 16232–16237.
46 V. Kumar, A. Y. S. Eng, Y. Wang, D.-T. Nguyen, M.-F. Ng and Z. W. Seh, *Energy Storage Mater.*, 2020, **29**, 1–8.
47 W. Luo, C. F. Lin, O. Zhao, M. Noked, Y. Zhang, G. W. Rubloff and L. Hu, *Adv. Energy Mater.*, 2017, **7**, 1601526.
48 Y. Zhao, L. V. Goncharova, A. Lushington, Q. Sun, H. Yadegari, B. Wang, W. Xiao, R. Li and X. Sun, *Adv. Mater.*, 2017, **29**, 1606663.
49 H. Wang, C. Wang, E. Matios and W. Li, *Nano Lett.*, 2017, **17**, 6808–6815.
50 D. Zhang, B. Li, S. Wang and S. Yang, *ACS Appl. Mater. Interfaces*, 2017, **9**, 40265–40272.
51 Y. Zhao, L. V. Goncharova, Q. Zhang, P. Kaghazchi, Q. Sun, A. Lushington, B. Wang, R. Li and X. Sun, *Nano Lett.*, 2017, **17**, 5653–5659.
52 S. Wei, S. Choudhury, J. Xu, P. Nath, Z. Tu and L. A. Archer, *Adv. Mater.*, 2017, **29**, 1605512.
53 Y.-J. Kim, H. Lee, H. Noh, J. Lee, S. Kim, M.-H. Ryou, Y. M. Lee and H.-T. Kim, *ACS Appl. Mater. Interfaces*, 2017, **9**, 6000–6006.
54 Y.-B. Niu, Y.-X. Yin, W.-P. Wang, P.-F. Wang, W. Ling, Y. Xiao and Y.-G. Guo, *CCS Chem.*, 2020, **2**, 589–597.
55 F.-Q. Liu, W.-P. Wang, Y.-X. Yin, S.-F. Zhang, J.-L. Shi, L. Wang, X.-D. Zhang, Y. Zheng, J.-J. Zhou, L. Li and Y.-G. Guo, *Sci. Adv.*, 2018, **4**, eaat5383.
56 J. Zhou, T. Qian, J. Liu, M. Wang, L. Zhang and C. Yan, *Nano Lett.*, 2019, **19**, 3066–3073.
57 Q. Zhao, X. Liu, S. Stalin, K. Khan and L. A. Archer, *Nat. Energy*, 2019, **4**, 365–373.
58 Y. Wang, C.-F. Lin, J. Rao, K. Gaskell, G. Rubloff and S. B. Lee, *ACS Appl. Mater. Interfaces*, 2018, **10**, 24554–24563.
59 C. Li, Q. Lan, Y. Yang, H. Shao and H. Zhan, *ACS Appl. Mater. Interfaces*, 2019, **11**, 2479–2489.
60 J.-L. Ma, F.-L. Meng, Y. Yu, D.-P. Liu, J.-M. Yan, Y. Zhang, X.-B. Zhang and Q. Jiang, *Nat. Chem.*, 2019, **11**, 64–70.
61 X. Zhang, Q. Zhang, X.-G. Wang, C. Wang, Y.-N. Chen, Z. Xie and Z. Zhou, *Angew. Chem., Int. Ed.*, 2018, **130**, 12996–13000.

62 Y.-X. Wang, W.-H. Lai, S.-L. Chou, H.-K. Liu and S.-X. Dou, *Adv. Mater.*, 2020, **32**, 1903952.
63 V. Kumar, Y. Wang, A. Y. S. Eng, M.-F. Ng and Z. W. Seh, *Cell Rep. Phys. Sci.*, 2020, **1**, 100044.
64 D. Aurbach, O. Youngman, Y. Gofer and A. Meitav, *Electrochim. Acta*, 1990, **35**, 625–638.
65 D. Aurbach, E. Pollak, R. Elazari, G. Salitra, C. S. Kelley and J. Affinito, *J. Electrochem. Soc.*, 2009, **156**, A694–A702.
66 V. Etacheri, U. Geiger, Y. Gofer, G. A. Roberts, I. C. Stefan, R. Fasching and D. Aurbach, *Langmuir*, 2012, **28**, 6175–6184.
67 Q. Liu, A. Cresce, M. Schroeder, K. Xu, D. Mu, B. Wu, L. Shi and F. Wu, *Energy Storage Mater.*, 2019, **17**, 366–373.
68 D. Aurbach, I. Weissman, A. Schechter and H. Cohen, *Langmuir*, 1996, **12**, 3991–4007.
69 H. Lee, D. J. Lee, Y.-J. Kim, J.-K. Park and H.-T. Kim, *J. Power Sources*, 2015, **284**, 103–108.
70 L. Lutz, D. Alves Dalla Corte, M. Tang, E. Salager, M. Deschamps, A. Grimaud, L. Johnson, P. G. Bruce and J.-M. Tarascon, *Chem. Mater.*, 2017, **29**, 6066–6075.
71 Z. Tu, S. Choudhury, M. J. Zachman, S. Wei, K. Zhang, L. F. Kourkoutis and L. A. Archer, *Nat. Energy*, 2018, **3**, 310–316.
72 C. Zhang, L. Shen, J. Shen, F. Liu, G. Chen, R. Tao, S. Ma, Y. Peng and Y. Lu, *Adv. Mater.*, 2019, **31**, 1808338.
73 K. Li, Y. Wang, W. Jia, S. Qu, Z. Yao, R. Cui, W. Zou, F. Zhou and J. Li, *ACS Appl. Mater. Interfaces*, 2020, **12**, 2285–2292.
74 H. Zhang, B. Qin, D. Buchholz and S. Passerini, *ACS Appl. Energy Mater.*, 2018, **1**, 6425–6432.
75 H. Zhang, B. Qin, J. Han and S. Passerini, *ACS Energy Lett.*, 2018, **3**, 1769–1770.
76 J. Sun, C. Guo, Y. Cai, J. Li, X. Sun, W. Shi, S. Ai, C. Chen and F. Jiang, *Electrochim. Acta*, 2019, **309**, 18–24.
77 F. Jiang, T. Li, P. Ju, J. Sun, C. Liu, Y. Li, X. Sun and C. Chen, *Nanoscale Adv.*, 2019, **1**, 4989–4994.
78 L. Jia, T. Wu, J. Lu, L. Ma, W. Zhu and X. Qiu, *ACS Appl. Mater. Interfaces*, 2016, **8**, 30248–30255.
79 Q. Li, Q. Wei, Q. An, L. Huang, W. Luo, X. Ren, K. A. Owusu, F. Dong, L. Li, P. Zhou, L. Mai, Q. Zhang, K. Amine and J. Lu, *Energy Storage Mater.*, 2018, **16**, 625–631.
80 H. Tao, Y. Tang, M. Zhou, R. Wang, K. Wang, H. Li and K. Jiang, *ChemElectroChem*, 2021, **8**, 157–163.